Dense granule trafficking in *Toxoplasma gondii* requires a unique class 27 myosin and actin filaments

Aoife T. Heaslip*, Shane R. Nelson, and David M. Warshaw*
Department of Molecular Physiology and Biophysics, University of Vermont, Burlington, VT 05405

ABSTRACT The survival of *Toxoplasma gondii* within its host cell requires protein release from secretory vesicles, called dense granules, to maintain the parasite's intracellular replicative niche. Despite the importance of DGs, nothing is known about the mechanisms underlying their transport. In higher eukaryotes, secretory vesicles are transported to the plasma membrane by molecular motors moving on their respective cytoskeletal tracks (i.e., microtubules and actin). Because the organization of these cytoskeletal structures differs substantially in *T. gondii*, the molecular motor dependence of DG trafficking is far from certain. By imaging the motions of green fluorescent protein–tagged DGs in intracellular parasites with high temporal and spatial resolution, we show through a combination of molecular genetics and chemical perturbations that directed DG transport is independent of microtubules and presumably their kinesin/dynein motors. However, directed DG transport is dependent on filamentous actin and a unique class 27 myosin, TgMyoF, which has structural similarity to myosin V, the prototypical cargo transporter. Actomyosin DG transport was unexpected, since filamentous parasite actin has yet to be visualized in vivo due in part to the prevailing model that parasite actin forms short, unstable filaments. Thus our data uncover new critical roles for these essential proteins in the lytic cycle of this devastating pathogen.

INTRODUCTION

Toxoplasma gondii infection causes congenital neurological defects and encephalitis in immunocompromised individuals (Nissapatorn, 2009; Oz, 2014). During an acute infection, parasites replicate in a specialized organelle within the host cell termed the parasitophorous vacuole (PV; Figure 1A). PV structure and stability are maintained through the parasite's release of proteins from secretory vesicles named dense granules (Coppens *et al.*, 2006; Travier *et al.*,

2008; Gold *et al.*, 2015; Figure 1A). Additional dense granule proteins that are released regulate host cell gene expression (Bougdour *et al.*, 2013, 2014; Braun *et al.*, 2013) and immune response (Pernas *et al.*, 2014; Rosowski *et al.*, 2014; Shastri *et al.*, 2014) and are thus essential for parasite survival and disease pathogenesis. Despite their importance, little is known about how dense granules are trafficked from their site of synthesis at the Golgi to release sites on the parasite's plasma membrane.

In mammalian cells, secretory vesicles formed at the Golgi are actively transported over long distances to the cell periphery by kinesin-1 molecular motors on microtubules (MTs). Once at the periphery, vesicles are handed off to actin-based myosin motors, such as myosin Va, which are believed to be involved in the final distribution and retention of vesicles within the actin-rich cell cortex (reviewed in Barral and Seabra, 2004; Park and Loh, 2008). In contrast, vesicle trafficking in budding yeast is exclusively actin based; actin cables serve as tracks for delivery of vesicles by myosin V motors to the mother-bud neck and bud tip (Pruyne *et al.*, 1998, 2004; Schott *et al.*, 2002). Thus the delivery of vesicles to the plasma membrane for secretion is dependent on molecular motors and their respective cytoskeletal tracks.

The organization of the MT and actin cytoskeletons in *T. gondii* differ dramatically from those in other eukaryotic cells, and so it is not known whether these cytoskeletal structures serve as tracks for dense granule transport by their associated molecular motors. *T. gondii* contains 23 highly stable, subpellicular MTs that originate at the apical end and run two-thirds the length of the parasite (Figure 1A; Morrissette *et al.*, 1997; Morrissette and Sibley, 2002a; Hu *et al.*, 2002). These MTs may provide a track for kinesin- and dynein-based dense granule transport. In contrast, parasite actin forms short, unstable filaments (Sahoo *et al.*, 2006; Skillman *et al.*, 2011) that have been implicated only in parasite motility and host cell invasion, processes distinct from secretory organelle transport (Carruthers and Boothroyd, 2007). However, actomyosin-based systems have recently been shown to be involved in the positioning of two other parasite secretory organelles, the micronemes and rhoptries, and in the inheritance of a plastid-like organelle, the apicoplast (Andenmatten *et al.*, 2013; Jacot *et al.*, 2013; Mueller *et al.*, 2013). Without any clear evidence for the presence of an organized, filamentous actin cytoskeleton in *T. gondii*, it is uncertain how myosin-based transport processes may be involved in dense granule transport.

With nothing currently known about the molecular mechanisms underlying dense granule transport and delivery to the plasma membrane, our goal was to determine how dense granules are trafficked within the parasite by defining granule motion dynamics through live-cell imaging and to discover whether MT- and actin-based molecular motor systems contribute to granule transport. To do this, we imaged and tracked the motions of fluorescently labeled dense granules with 20 nm spatial and 100 ms temporal resolution. Dense granules exhibit predominantly directed motion (indicative of an active process) or random, diffusive-like motion. Only a small proportion of granules were stationary. Surprisingly, depolymerization of the parasite's MTs had no effect on these modes of granule motion or their probability. Directed dense granule motion was nearly ablated following the loss of putative actin filaments, either through depolymerization or actin knockout, suggesting that actin filaments in the parasite's cytosol do exist and serve as tracks for dense granule transport by a yet to be identified myosin motor. On the basis of the striking structural similarity of a class 27, parasite myosin motor, TgMyoF, to one of the most well-characterized cargo transporters, myosin Va, we generated a parasite line in which full-length TgMyoF was replaced with a mutant, C-terminal–truncated TgMyoF (*TgMyoF-ΔCT*). The loss of functional TgMyoF led to a similar dramatic reduction in directed dense granule motion as observed with the loss of actin. In all, this study reveals an unexpected MT-independent but actomyosin-dependent transport mechanism for dense granules.

RESULTS

Imaging dense granule motions in intracellular parasites

To elucidate the molecular mechanisms underlying dense granule trafficking in *T. gondii*, we imaged dense granule motions in intracellular parasites growing inside the PV ~18 h postinvasion. Granules were fluorescently labeled by ectopically expressing the enhanced green fluorescent protein (eGFP)-labeled surface antigen SAG1 with its glycosylphosphatidylinositol (GPI) anchor signal sequence removed (SAG1ΔGPI-GFP). This truncated protein mislocalizes to the dense granule lumen and is subsequently secreted into the PV (Figure 1B and Supplemental Figure S1; Striepen *et al.*, 1998). Granule motions were highly dynamic, with the majority of granules demonstrating either directed or random, diffusive-like motion (Supplemental Movie S1). Many granules were observed to switch between these two distinct modes of motion, as previously described for insulin granules and endosomal vesicles in mammalian cells (Zajac *et al.*, 2013; Heaslip *et al.*, 2014). Interestingly, some granules moved bidirectionally, that is, directed runs abruptly reversed direction (Supplemental Figure S2A). For full characterization and quantification of granule motion dynamics, granules were tracked, and the resultant trajectories were analyzed using methodology we previously developed for analyzing the complex nature of insulin granule motions in pancreatic beta-cells (Heaslip *et al.*, 2014; *Materials and Methods*). Using mean square displacement (MSD)
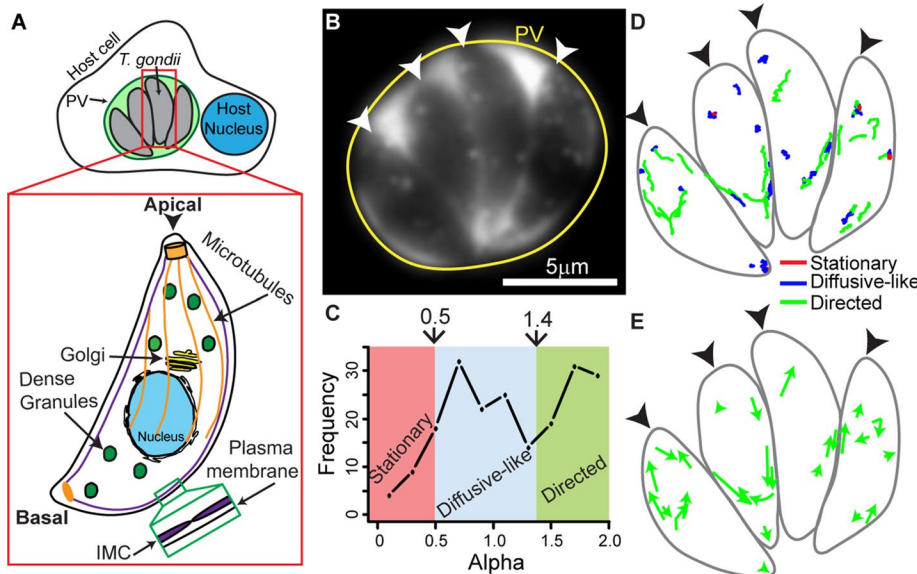
FIGURE 1: Characterization of dense granule motions in *T. gondii*. (A) Cartoon showing four *T. gondii* parasites growing inside a PV in a host cell. Inset shows cytoskeletal structures and organelles in *T. gondii* referred to in the text. Parasites contain 23 MTs (orange) that run two-thirds the length of the parasite, a single Golgi stack (yellow), and dense granules (green) distributed throughout the parasite. The inner membrane complex (IMC; green inset) is a series of flattened vesicles that are sutured together and underlie the parasite's plasma membrane. The apical end of the parasite is indicated with an arrowhead. (B) Image of a four-parasite PV (yellow circle) with eGFP-labeled dense granules. eGFP accumulates in the PV after dense granule secretion. The apical end of each parasite is indicated with a white arrowhead. (C) Frequency distribution of MSD alpha values in control parasites. Trajectories with an $\alpha < 0.5$ are classified as stationary (red), trajectories with an α between 0.5 and 1.4 are classified as diffusive-like (blue), and trajectories with an $\alpha > 1.4$ are classified as directed (green). (D) Outline of parasites shown in B, with dense granule trajectories overlaid. Directed granule trajectories are indicated in green, diffusive-like trajectories are indicated in blue, and stationary trajectories are indicated in red. (E) Outline of parasites shown in B with directed dense granule trajectories in D depicted as arrows to highlight directionality. In D and E, black arrowheads indicate the parasites' apical ends.
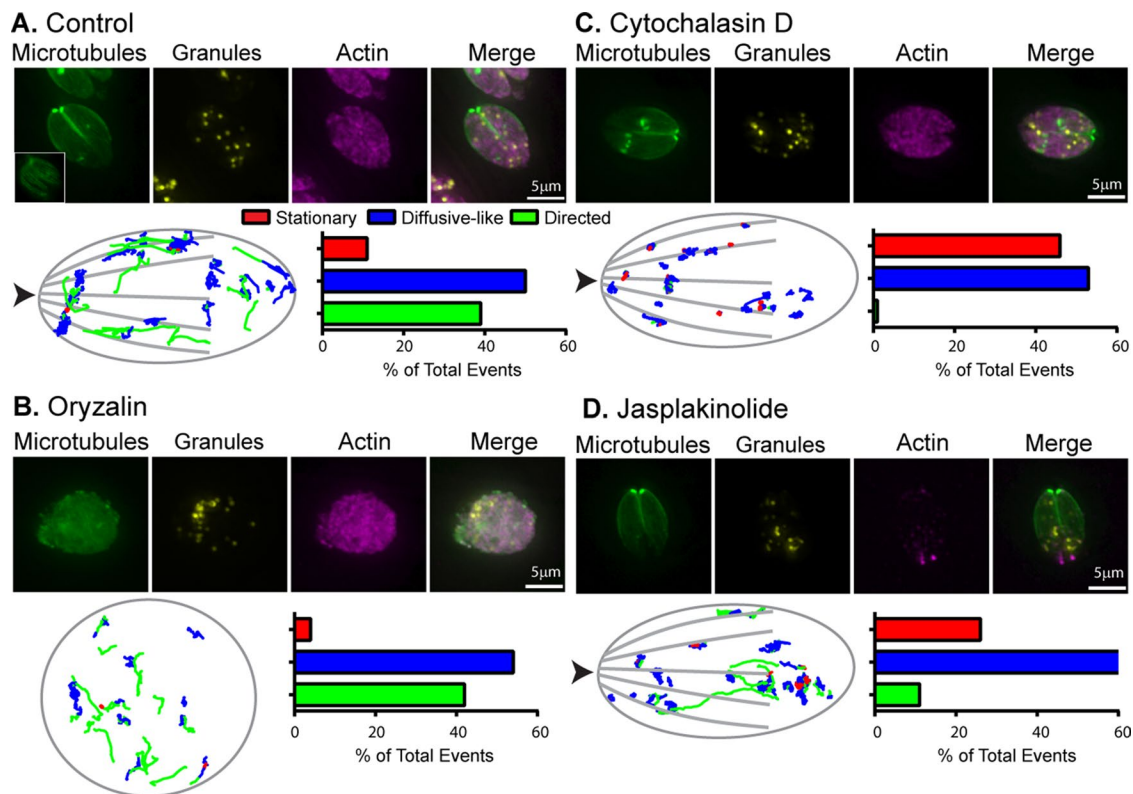
FIGURE 2: Parasite actin but not MTs are necessary for directed dense granule transport. (A–D) Top, fluorescence images of control and oryzalin-, cytochalasin D–, and jasplakinolide-treated parasites. Green: mCherryFP-tubulin; yellow: SAG1-ΔGPI-eGFP to identify dense granules; pink: anti-actin. (A–D) Bottom, left, generic parasite outline with dense granule trajectories from 10 parasites overlaid; trajectories from five vacuoles were overlaid for oryzalin. Images were overlaid based on the *x,y* coordinates of the apical and basal ends of each parasite. Arrowhead indicates parasite's apical end. Right, bar chart showing the percentage of granules exhibiting stationary (red), diffusive-like (blue), and directed (green) motion in each condition. See Supplemental Table S1 for trajectory specifics.

analysis, we calculated the diffusive exponent, α, of each trajectory, which allowed us to categorize granules into either stationary (α < 0.5), diffusive-like (0.5 ≥ α ≤ 1.4), or directed (α > 1.4) populations (Figure 1C and Supplemental Figure S2B).

In intracellular parasites, 39% of dense granules moved in a directed manner with a velocity of 486 ± 19 nm/s and a run length of 715 ± 82 nm (Figures 1D and 2A and Supplemental Table S1). Fifty percent of granules moved in a diffusive-like manner, with diffusion coefficients of 3135 ± 110 nm²/s. Only 11% of granules were stationary. Because our goal was to characterize the active motor-driven mechanisms underlying granule transport, the location and directionality of the directed granule motions were analyzed. Directed granule motions occurred predominantly at the parasite's periphery, with 59% occurring at the apical end of the parasite and the remainder occurring at the basal end of the parasite, which is devoid of MTs (Figure 1E and Supplemental Movie S1). We observed no bias in relation to directionality of the directed motions; granules moved with approximately equal frequency toward the apical and basal ends of the parasite (Figure 1E and Supplemental Figure S2C).

MTs are not required for directed dense granule motion
The presence of directed dense granule motion implies that a significant component of granule trafficking may be dependent on molecular motor transport. If so, then directed granule motion should be susceptible to perturbations of the cytoskeletal tracks on which the motors travel. To determine whether parasite MTs were

necessary for directed granule transport, we depolymerized MTs using oryzalin, a compound that disrupts plant but not vertebrate or fungal MTs (Shaw *et al.*, 2000; Morrissette and Sibley, 2002b; Morrissette *et al.*, 2004). Oryzalin treatment disrupts the parasite's polarized cytoskeletal organization and results in parasite masses inside the PV (Shaw *et al.*, 2000; Figure 2B, top panel). Despite the dramatic effect on parasite morphology, oryzalin treatment had no effect on the percentage of granules in stationary, diffusive-like, and directed populations (Figure 2B, bottom panel, and Supplemental Movie S2). Directed granule run lengths remained unchanged, while there was a modest decrease in directed granule velocities from 486 ± 19 nm/s in control cells to 391 ± 19 nm/s in oryzalin-treated cells (Supplemental Table S1). Collectively these data show that MTs are not required for dense granule–directed motion and, therefore, transport by MT-based molecular motors.

Directed dense granule motions are actin dependent
We next sought to determine whether the actin cytoskeleton was required for dense granule transport. However, as previously reported, filamentous actin was not apparent in immunofluorescence images of parasites stained with an antiparasite actin antibody (Figure 2A; Skillman *et al.*, 2011; Andenmatten *et al.*, 2013). Thus it was not surprising that actin filament depolymerization with cytochalasin D had no observable effect on the actin localization or structural appearance compared with controls (Figure 2C, top panel). Despite the lack of change in actin structure, cytochalasin D

treatment ablated directed granule motion, given that only 1% of granules retained this behavior (Figure 2C, lower panel, and Supplemental Movie S2), with a concomitant increase in the percentage of granules in the diffusive-like and stationary populations. Diffusion coefficients of diffusive-like granules also dropped by 70% from 3135 ± 110 nm^2/s in control cells to 835 ± 53 nm^2/s in cytochalasin D–treated cells. This result is consistent with directed granule motion and transport being an actin-dependent process. We then assessed the effect of jasplakinolide treatment, a disruptor of actin dynamics, on dense granule motion (Bubb et al., 1994, 2000). Following jasplakinolide treatment, filamentous actin structures were not apparent, but punctate spots appeared at the basal end of the parasites, which was in contrast to the diffuse staining seen in control parasites (Figure 2, A and D; Haase et al., 2015). Jasplakinolide treatment resulted in an eightfold decrease in percentage of granules undergoing directed motion (Figure 2D and Supplemental Movie S2). In addition, directed granule run lengths were 50% shorter (321 ± 130 nm vs. 715 ± 82 nm) and 60% slower (190 ± 12 nm/s vs. 486 ± 19 nm/s) after jasplakinolide treatment compared with controls (Supplemental Table S1). Diffusion coefficients of diffusive-like granules were also 50% slower at 1586 ± 63 nm^2/s (compared with 3135 ± 110 nm^2/s in controls).

To further confirm that directed dense granule transport is an actin-dependent process, we imaged dense granule motions in a conditional actin knockout parasite line, LoxP-actin (Andenmatten et al., 2013). In this parasite line, the TgACT1 gene is flanked by two LoxP sites. On the induction of a functional Cre recombinase using rapamycin (Figure S3A; Andenmatten et al., 2013), the actin-coding sequence is removed from the parasite's genome and repositions the yellow fluorescent protein (YFP) coding sequence adjacent to a constitutively active promoter. Untreated LoxP-actin parasites expressing SAG1-ΔGPI-mCherryFP display dense granule dynamics indistinguishable from untreated control parasites expressing SAG1-ΔGPI-eGFP (compare Figures 2A and 3A). However, 65 h after rapamycin treatment, actin-deficient, YFP-positive parasites have a fivefold reduction in the percentage of granules moving in a directed manner (i.e., from 35 to 7%) compared with untreated LoxP-actin controls (Figure 3, A and B, and Supplemental Movie S3). The percentage of granules in stationary and diffusive-like populations increased from 12 to 32% and 53 to 61%, respectively (Supplemental Table S1). There was also a twofold decrease in directed granule velocities and run lengths and a twofold decrease in diffusion coefficients of diffusive-like granules (Supplemental Table S1). Loss of parasite actin also had a modest effect on the dense granule inheritance/biogenesis, with ~20% of vacuoles containing at least one parasite in which no dense granules were observed (Supplemental Figure S3B). Collectively these experiments show that actin and its state of polymerization are necessary for directed dense granule transport.

TgMyoF is required for directed dense granule transport

The presence of actin-dependent, directed granule motion implicates myosin molecular motor involvement. The most well-studied vesicular cargo transporter is the class V motor, myosin Va (reviewed by Trybus, 2008; Hammer and Sellers, 2012). Myosin Va has a conserved motor domain that binds actin and hydrolyzes ATP, a long neck region or lever arm that contains six calmodulin-binding IQ motifs, a coiled-coil domain for dimerization, and a globular tail that binds cargo (Figure 4A). Of the 10 myosin genes in T. gondii (Foth et al., 2006), only a single myosin, TgMyoF, has putative structure similar to myosin Va (Figure 4A). TgMyoF is a class 27 myosin motor (Odronitz and Kollmar, 2007), and its motor domain and lever arm share 35% amino acid–sequence identity with mouse myosin Va
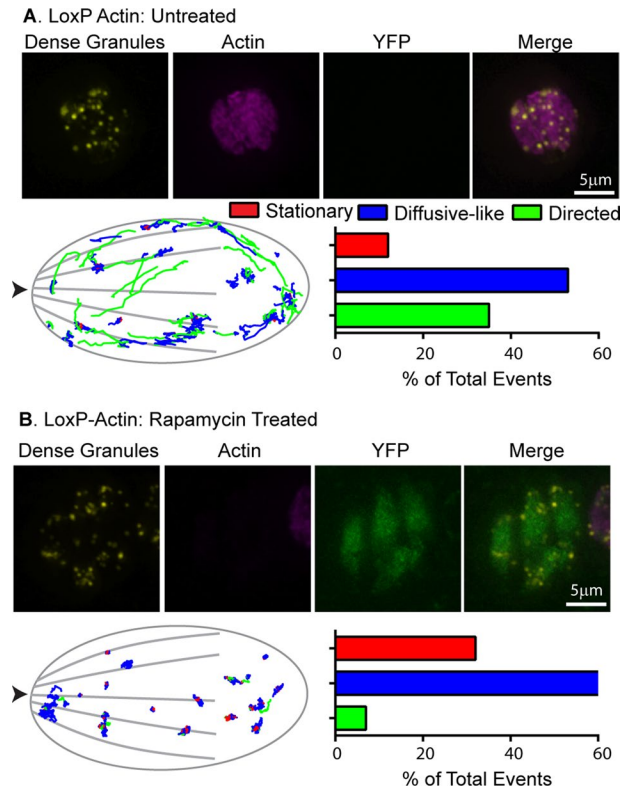

FIGURE 3: Loss of TgACT1 perturbs directed dense granule motions. (A and B) Top, fluorescence images of control and rapamycin-treated LoxP-Actin parasites. Yellow: SAG1-ΔGPI-eGFP to identify dense granules; pink: anti-actin; green: YFP. (A and B) Bottom, left, parasite outline with dense granule trajectories from 10 parasites overlaid. Images were overlaid based on the x,y coordinates of the apical and basal ends of each parasite. Arrowhead indicates parasite's apical end. Right, bar chart showing the percentage of granules exhibiting stationary (red), diffusive-like (blue), and directed (green) motion in each condition. See Supplemental Table S1 for trajectory specifics.

(Supplemental Figure S4, A and B). TgMyoF contains a coiled-coil domain that is approximately one-third the length of the coiled-coil domain of myosin Va (Supplemental Figure S4C). At its C-terminus, TgMyoF has a putative WD40 β-propeller domain (Foth et al., 2006). Taken together, these structural features suggest that TgMyoF is a
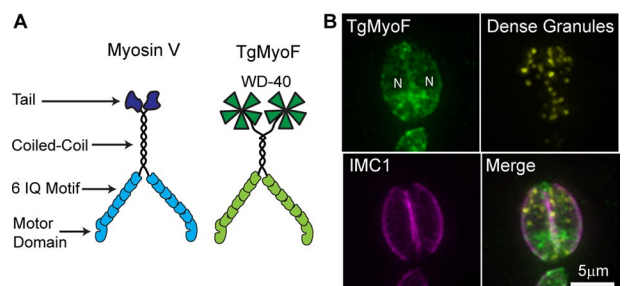
FIGURE 4: Comparison of TgMyoF structure with myosin Va and localization of TgMyoF. (A) Depiction of myosin Va and putative TgMyoF structure. (B) Fluorescence image of a two-parasite vacuole showing TgMyoF localization in the parasite's cytosol. TgMyoF is excluded from the parasite's nucleus (N). Images are maximum-intensity projections of deconvolved images. Green: endogenous TgMyoF-emeraldFP; yellow: SAG1-ΔGPI-mCherryFP to identify dense granules; pink: anti-IMC1.
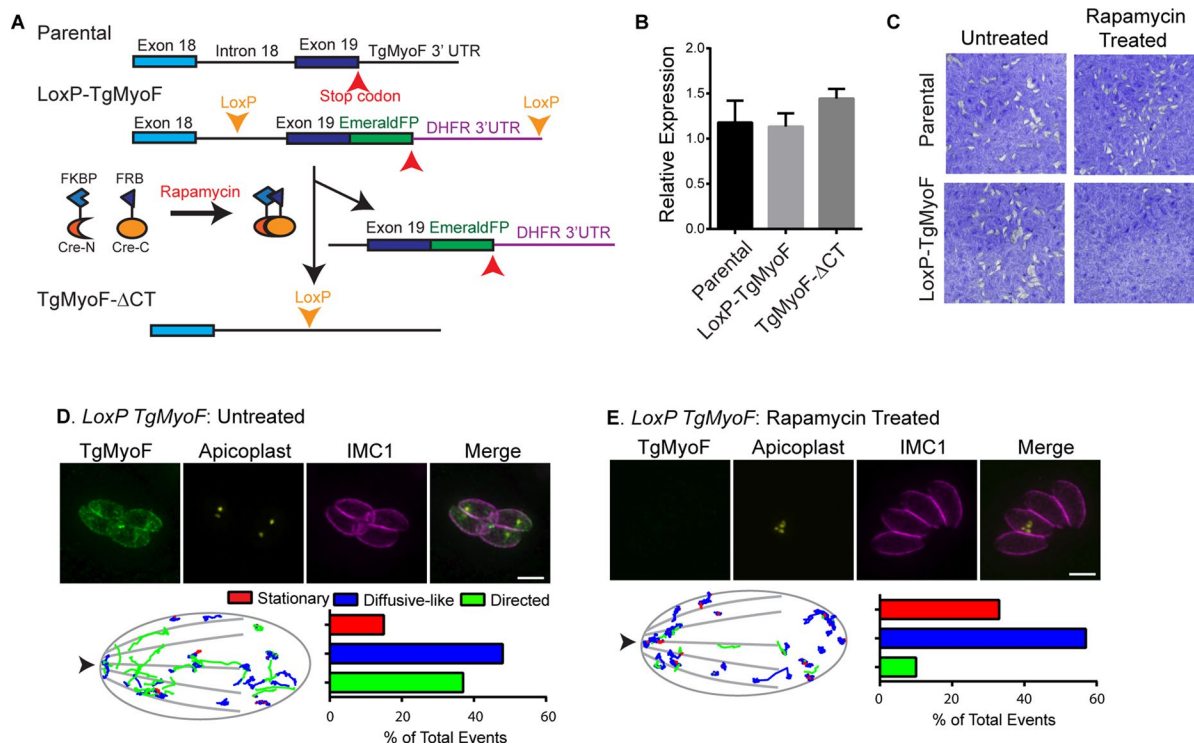
FIGURE 5: TgMyoF is required for directed dense granule motion. (A) Strategy for creating *LoxP-TgMyoF* and *TgMyoF-ΔCT* parasite lines. See the text for details. (B) Relative expression levels of full-length TgMyoF in parental and untreated *LoxP-TgMyoF* parasites compared with the expression level of TgMyoF-ΔCT in rapamycin-treated *LoxP-TgMyoF* parasites assessed using qPCR. (C) Growth of parental and *LoxP-TgMyoF* parasite lines as assessed by plaque assay with and without rapamycin treatment. (D and E) Top, fluorescence image of control and rapamycin-treated *LoxP-TgMyoF* parasites indicating aberrant apicoplast inheritance in TgMyoF-deficient parasites. Green: TgMyoF-emeraldFP; yellow: TgFNR-RFP highlighting the apicoplast; pink: anti-IMC1. (D and E) Bottom, left, parasite outline with dense granule trajectories from 10 parasites overlaid. Images were overlaid based on the *x,y* coordinates of the apical and basal ends of each parasite. Arrowhead indicates parasite's apical end. Right, bar chart showing the percentage of granules exhibiting stationary (red), diffusive-like (blue), and directed (green) motion in each condition. See Supplemental Table S1 for trajectory specifics.

potential candidate motor to transport dense granules on actin tracks. When the endogenous *TgMyoF* gene was C-terminally tagged with emeraldFP, the protein exhibited a diffuse cytosolic localization (Figure 4B; Jacot *et al.*, 2013).

For assessing the role of TgMyoF in dense granule trafficking, a *LoxP-TgMyoF* parasite line was created. Using the *Ku80::diCre* parental line (Andenmatten *et al.*, 2013), the *LoxP-TgMyoF* line was created by tagging the last exon (exon 19) of TgMyoF with emeraldFP, which was immediately followed by the 3′ UTR of the *DHFR* gene. Exon 19, emeraldFP, and the 3′ UTR were flanked by LoxP sites (Figure 5A and Supplemental Figure S5, A and B). On induction of an inducible Cre recombinase with rapamycin, the removal of the DNA between the LoxP sites results in a parasite line that no longer expresses full-length TgMyoF as evidenced by the loss of emeraldFP fluorescence (Figure 5, D and E, and Supplemental Figure S5C). For determination of whether removal of the last exon of Tg-MyoF and its 3′ UTR resulted in a true TgMyoF-null parasite line or whether a C-terminal, truncated TgMyoF transcript (*TgMyoF-ΔCT*) was still expressed in these cells, TgMyoF transcript expression was assessed using quantitative PCR (qPCR) in the parental line and the *LoxP-TgMyoF* line without rapamycin treatment compared with the level of *TgMyoF-ΔCT* transcript expression following rapamycin treatment of the *LoxP-TgMyoF* line. After rapamycin treatment, ~60% of *LoxP-TgMyoF* parasites had undetectable levels of Tg-

MyoF-emeraldFP as assessed by an immunofluorescence assay. However, the levels of the mutant TgMyoF transcript equaled that of the full-length TgMyoF in untreated *LoxP-TgMyoF* and parental lines (Figure 5B). To evaluate how expression of the mutant *TgMyoF-ΔCT* affected parasite viability, we performed a plaque assay with parental and *LoxP-TgMyoF* parasites with and without rapamycin treatment. Growth of parental parasites was unaffected by rapamycin treatment, while treatment of *LoxP-TgMyoF* line resulted in little plaque formation, and the few plaques that did form were TgMyoF-emeraldFP positive, indicating that loss of the C-terminus of TgMyoF rendered the protein nonfunctional (Figure 5C). Consistent with this, *TgMyoF-ΔCT* parasites exhibited aberrant apicoplast inheritance and microneme accumulation in the residual body, as expected (Jacot *et al.*, 2013; Figure 5, D and E, upper panels, and Supplemental Figure S5C), and to date we have been unable to isolate a stable *TgMyoF-ΔCT* parasite line. For determination of whether the growth defect in the *TgMyoF-ΔCT* parasites could be solely attributed to the apicoplast inheritance defect, a replication assay was performed, and the number of parasites/vacuole 40 h after invasion was determined. Although the apicoplast is an essential organelle, mutant parasites that contain only one apicoplast per vacuole can grow at similar rates to wild-type parasites (He *et al.*, 2001). However, *TgMyoF-ΔCT*/apicoplast positive (vacuoles that contain at least one apicoplast) and *TgMyoF-ΔCT*/apicoplast

negative (zero apicoplast/vacuole) exhibit equally severe replication defects (Supplemental Figure S7). Thus we conclude that the apicoplast inheritance defect cannot fully account for the lethality of the *TgMyoF-ΔCT* parasite line.

For determination of whether TgMyoF plays a role in directed dense granule transport, mCherryFP-labeled dense granule motions were imaged in *LoxP-TgMyoF* parasites ~60 h after rapamycin treatment when TgMyoF-emeraldFP is undetectable in ~60% of parasite vacuoles. *TgMyoF-ΔCT* parasites exhibit a fourfold decrease in the proportion of granules exhibiting directed motion compared with the untreated *LoxP-TgMyoF* controls (Figure 5, D and E, and Supplemental Movie S4). In addition, following rapamycin treatment, there were a fourfold decrease in directed granule run lengths (198 ± 66 nm vs. 813 ± 124 nm) and a 50% decrease in directed dense granule velocities (172 ± 9 nm/s vs. 443 ± 22 nm/s). A 50% decrease in the diffusion coefficients of the diffusive-like granules was also observed (901 vs. 2202 nm^2/s compared with controls; Supplemental Table S1).

DISCUSSION

Intracellular cargo transport is vital for the timely and efficient delivery of secretory vesicles to the plasma membrane for secretion. Given the importance of dense granule secretion to disease pathogenesis by *T. gondii*, the goal of this study was to determine whether and how the unusual MT and putative actin cytoskeletons in *T. gondii* are required for trafficking dense granules to the plasma membrane. We hypothesized that the stable and highly organized MTs would provide an excellent track for kinesin- and/or dynein-based dense granule transport. Surprisingly, MT depolymerization using oryzalin had no effect on the proportion of dense granules moving in a directed manner. Instead, dense granule transport was entirely actin dependent; that is, loss of actin filaments, either through depolymerization or actin protein knockout, resulted in an almost complete ablation of directed granule motion. In addition, loss of functional TgMyoF, a class 27 myosin motor with a putative structure reminiscent of the well-characterized cargo transporter myosin Va also resulted in a dramatic decrease in directed granule transport.

Our data support an actomyosin-based mechanism for dense granule transport in *T. gondii*. Such a mechanism was unexpected, given the large body of literature showing that actin from apicomplexan parasites forms short and unstable filaments (Sahoo *et al.*, 2006; Skillman *et al.*, 2011) that cannot be visualized in *T. gondii* (see Figure 2) and given the assumption that much of the parasite's actin is believed to be in the globular form (Dobrowolski *et al.*, 1997). In fact, these data are the basis for the prevailing model in the field, in which actin filaments are only transiently formed at the parasite's periphery during parasite motility and invasion (Baum *et al.*, 2006, 2008; Carruthers and Boothroyd, 2007; Besteiro *et al.*, 2011). At a minimum, our data suggest that TgMyoF must transport dense granules along filamentous actin structures even if those structures cannot be visualized, given that myosin is only capable of actin-activated ATPase activity or force and motion generation by interacting with filamentous actin (Figure 6A). It is possible that parasite actin-binding proteins such as formin, profilin, and coronin may coordinate their activities in vivo to produce longer actin filaments than those formed in vitro and thus create an ideal track for TgMyoF-based dense granule transport. As evidence, TgACT1 does form longer filaments, bundles, and meshworks in the presence of these actin-binding proteins in vitro (Skillman *et al.*, 2012; Salamun *et al.*, 2014; Olshina *et al.*, 2015). In addition, loss of actin-depolymerizing factor 1 affects actin-based apicoplast inheritance but not actin-based parasite motility and invasion, suggesting that different actin-
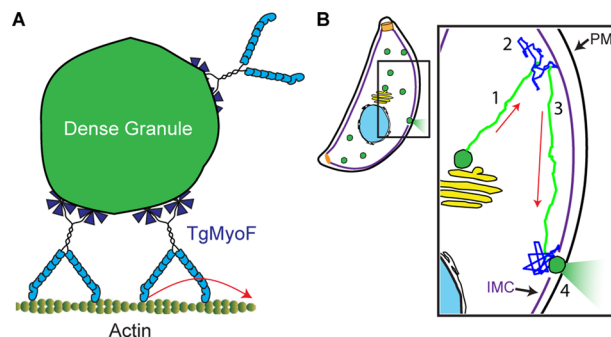
FIGURE 6: Model of dense granule trafficking. (A) Teams of TgMyoF motors interact with the granule surface via their WD40 domains and can move processively (i.e., take consecutive steps without dissociating) along actin tracks. (B) Model of TgMyoF and actin-based dense granule transport and sites of secretion: 1) Dense granules (green) formed at the Golgi (yellow) are transported (green trajectory) by TgMyoF motors along actin tracks to the parasite's periphery. 2) Once at the periphery, diffusive-like motion (blue squiggle) provides a means to rapidly probe a small area of the IMC for a potential IMC gap and access to a docking site. 3) Dense granules that have yet to dock on the plasma membrane (PM) can once again undergo TgMyoF-directed transport (green trajectory) on filamentous actin parallel to the IMC. Once directed motion terminates, the granule is again free to move in a diffusive manner (blue squiggle) in search of a plasma membrane docking site. 4) An encounter with an IMC gap and access to the plasma membrane allows dense granule docking and secretion. Red arrows indicate the direction of directed granule motion.

binding proteins could control the formation of higher-order actin structures suited to different biological processes (Haase *et al.*, 2015). Until such time that the molecular toolbox expands to imaging filamentous actin in *T. gondii*, we can only assume that a filamentous actin network exists throughout the entire parasite and facilitates directed granule transport. Given the structural similarity between TgMyoF and myosin Va, we hypothesize that TgMyoF motors are bound to the granule surface through their WD40 domains and transport their cargo by walking on the filamentous actin cytoskeleton (Figure 6A). Future experiments will be required to further elucidate the molecular mechanisms of trafficking. Because TgMyoF does not appear to be concentrated on the dense granule surface (Figure 4B), we cannot at this point exclude the possibility that another, as yet uncharacterized myosin motor is also involved in transport or that TgMyoF might play an alternate role in trafficking, such as cross-linking actin filaments through its WD40 domain (WD40 domains are found in a number of actin-binding proteins, including coronins; Xu and Min, 2011).

In addition to its putative role in dense granule transport, TgMyoF is required for apicoplast inheritance and anchoring of the micronemes and rhoptries at the parasite's apical end (Jacot *et al.*, 2013; Mueller *et al.*, 2013). Thus TgMyoF's dual roles in transport and anchoring are reminiscent of mammalian myosin VI, which transports endocytic vesicles and anchors actin filaments to the plasma membrane at the base of stereocilia (reviewed by Frank *et al.*, 2004; Sweeney and Houdusse, 2007; Tumbarello *et al.*, 2013). Myosin VI has a 35 amino-acid insert (insert 1) in its motor domain that slows both ADP release and ATP binding during the catalytic cycle and is thought to be important for the load-induced switching between the motor's transporting and anchoring roles (Altman *et al.*, 2004; Menetrey *et al.*, 2005; Chuan *et al.*, 2011). Sequence alignment of the TgMyoF motor domain with the motor domains

from class V, VI, VII, and X myosins show that TgMyoF contains three unique inserts ranging in size from 9 to 22 amino acids (Supplemental Figure S4A). These inserts are in similar (although not identical) locations to insert I in myosin VI and adjacent to switch-1, loop-1, and P-loop; sequences involved in nucleotide binding and release. Future work is needed to determine how TgMyoF's unique inserts affect the motor's biophysical properties and whether they enable TgMyoF to perform these functionally distinct roles in secretory organelle transport and anchoring.

Given that dense granule motions in *T. gondii* are predominantly diffusive-like and directed, we hypothesize that these two modes of motion both contribute to successful trafficking of granules from their site of synthesis to release sites on the parasite's plasma membrane. Loss of either actin or a functional TgMyoF reduced both the proportion of directed granule motions and the diffusion coefficients of diffusive-like granules. This reduction in diffusion coefficients suggests that, in addition to the passive diffusive motions that solely rely on thermal energy, a proportion of diffusive-like motions are due to granules being transported by TgMyoF on a randomly oriented cytoskeletal actin network, as seen previously for myosin Va motors in COS-7 cells (Nelson *et al.*, 2009). Diffusive-like motion (regardless of the underlying mechanism) provides a mechanism for short-range motions (<microns), whereas directed, motor-driven transport offers the advantage of covering longer distances (>microns) in shorter time frames but requires energy derived from ATP hydrolysis. Therefore we propose that newly synthesized dense granules are transported from the Golgi to the parasite's periphery by TgMyoF motors moving along filamentous actin (Figure 6B). However, once at the periphery, the dense granules have an unusual obstacle to overcome before they reach the plasma membrane for secretion—namely, the inner membrane complex (IMC), a series of flattened vesicles that are sutured together and located underneath the plasma membrane (Figure 1A; reviewed by Harding and Meissner, 2014). Electron microscopic images suggest that the granules do not fuse to the IMC itself (Dubremetz *et al.*, 1993) for secretion but rather must traverse the IMC through small gaps in the IMC plates. To find these IMC gaps, granule diffusion would provide a means of rapidly probing a small area at the parasite's periphery. If the granule does not encounter a potential exit site, then the granule and its bound TgMyoF motors could initiate a directed run parallel to the IMC. The run terminates when the granule falls off its actin filament track, and the granule is free to begin another local search using diffusive movements to successfully encounter an IMC exit site, resulting in eventual dense granule content secretion. Future work is required to determine how and where dense granules traverse the IMC during the secretory process and how loss of directed granule transport affects dense granule secretion.

Given TgMyoF's important biological functions, it is not surprising that a stable *TgMyoF-ΔCT* parasite line could not be isolated. MyoF is conserved in other apicomplexan parasites of significant medical importance such as *Plasmodium* spp. the causative agent of malaria (Foth *et al.*, 2006; Jacot *et al.*, 2013). Thus both TgMyoF and the parasite's actin cytoskeleton may be suitable targets for the development of antiparasitic drugs.

MATERIALS AND METHODS
Tissue culture and parasite transfection
T. gondii tachyzoites derived from RH strain were used in all experiments. Parasites were maintained by continuous passage in human foreskin fibroblasts (HFFs) in DMEM containing 1% (vol/vol) heat-inactivated fetal bovine serum (FBS), 1× antibiotic/antimycotic as previously described (Roos *et al.*, 1994). All reagents were purchased from Life Technologies (Carlsbad, CA). Parasites were transfected as described previously (van den Hoff *et al.*, 1992) using a BTX electroporation set as follows: voltage, 1500 V; resistance, 25 Ω; and capacitance, 25 μF.

Construction of expression plasmids
Creation of ptub-SAG1ΔGPI-GFP and ptub-SAG1ΔGPI-mCherryFP. The first 861 base pairs (out of 1011 base pairs total) of the *SAG1* gene was amplified by PCR using an RH parasite cDNA library (isolated as previously described in Hu *et al.*, 2006) as a template and NheI-SAG1F/BglII-SAG1-287R primers (Supplemental Table S2). The resulting PCR product, which encodes the first 287 amino acids of the *SAG1* gene, was subcloned using NheI and BglII restriction sites into the ptub-mCherryFP-eGFP and ptub-eGFP-mCherryFP plasmids respectively (kind gifts from Ke Hu, Indiana University, Bloomington) to yield ptub-SAG1ΔGPI-GFP and ptub-SAG1ΔGPI-mCherryFP.

Creation of pTKO2_II_3_MyoF_emeraldFP plasmid. The last 1536 base pairs of the TgMyoF genomic locus were cloned by GenScript (Piscataway, NJ) into a pUC57 vector to create pUC57-TgMyoF-3'. In the middle of intron 18, a 66 base pair sequence was inserted that contains the 34 base pair LoxP site (gagctcgcggccgcataacttcgtata-GCATACATtatacgaagttatgaattccaattgggtacc; 13 base pair recognition sequences are underlined, and 8 base pair spacers are highlighted by block capitals). BamHI/BssHII sites on the pUC57-TgMyoF-3' plasmid were used to subclone TgMyoF-3' into the pTKO2_II_mCherry plasmid described in Liu *et al.* (2013), which was digested with BglII and BssHII. All plasmid sequences were confirmed using DNA sequencing.

Dense granule imaging, tracking, and movement analysis
Parasite lines and drug treatments. For creation of a parasite line containing GFP-labeled dense granules (i.e., stably expressing SAG1ΔGPI-GFP), 40 μg the ptub-SAG1ΔGPI-GFP plasmid was transfected into 1 × 10⁷ RH parasites as described in the previous section. Transfected parasites were selected using 6 μg/ml chloramphenicol until >80% of parasites were GFP positive. A clonal line was isolated by limited dilution in a 96-well plate. For assessing the effect of actin perturbation on dense granule motions, intracellular parasites were treated with 2 μm cytochalasin D or 1 μm jasplakinolide for 60 min before dense granule motions were imaged. For depolymerization of parasite MTs, intracellular parasites were grown in the absence of drug for 2 h postinvasion and then grown in the presence of 2.5 μm oryzalin for 24 h before imaging. For determination of whether depletion of actin or TgMyoF affects dense granule motions, parasites were allowed to invade confluent HFF monolayers for 4 h before treatment with 0.5 μM rapamycin for 30 min. Parasites were grown in drug-free DMEM for ~48 h until parasites lysed the HFF monolayer, after which 1 × 10⁷ parasites were transfected with 40 μg ptub-SAG1-ΔGPI-mCherryFP plasmid before being added to MatTek dishes (MatTek Corporation, Ashland, MA) containing confluent HFF monolayers and grown for a further 12–18 h before granule motions were imaged as described above. For imaging of granules from fixed cells, SAGΔGPI-GFP parasites were grown overnight in MatTek dishes containing confluent HFF monolayers, and the cells were washed once in 1× PBS and then fixed with 4% paraformaldehyde/1× PBS for 15 min at room temperature. Cells were washed three times in 1× PBS and imaged and tracked as described in the following section.

Granule imaging and tracking. Intracellular parasites were imaged ~18 h after invasion into confluent HFF monolayers grown on MatTek dishes. Growth media was replaced with Fluorobrite DMEM (Life Technologies) containing 1% FBS and 1× antimycotic/antibiotic prewarmed to 37°C. Images were acquired using a Nikon Ti-E inverted microscope with a 100×, 1.49 NA objective in an environmental chamber heated to 37°C equipped with an Spectra-X light engine (Lumencore, Beaverton, OR) and a Clara cooled charge-coupled device camera (Andor, South Windsor, CT). Images were acquired at 100 ms for 1 min. Dense granule motions were tracked using the ImageJ, version 1.43, plug-in, SpotTracker2D (National Institutes of Health), allowing us to determine the granules' positions at subpixel resolution in every frame of the movie so that change point and MSD analysis could be performed (see following section). Out-of-focus granules and granules that could not be spatially resolved from one another were eliminated from analysis. When necessary, the ImageJ plug-in "template matching" was used to compensate for drift of the PV inside the cell.

MSD and change point analysis. Granule trajectories were segmented into "directed," "diffusive-like," and "stationary" periods using a "change point" algorithm implemented through custom scripts written in R, a programming language and environment for statistical analysis (Heaslip *et al.*, 2014). This algorithm uses a rolling-window MSD analysis to provide an unbiased approach to identifying distinct modes of motion within a single trajectory. The mode of motion exhibited by each segment was characterized by plotting the MSD versus time (*dT*) relationship on a log–log axis (Supplemental Figure S2B). The slope defined the diffusive exponent, α, where in general $\alpha \sim 0$ was characteristic of a stationary granule, $\alpha \sim 1$ indicated diffusive-like motion, and $\alpha \sim 2$ was indicative of directed motion (Saxton, 1997). Segmenting and subsequent analysis by MSD was performed as previously described (Heaslip *et al.*, 2014) with the following modifications: 1) Directed motions were defined by $\alpha > 1.4$ based on simulated data and a clear minimum in the α distribution at 1.4 (Figure 1C). Stationary granules were defined by $\alpha < 0.5$ based on MSD analysis of granules in fixed cells, which resulted in $\alpha = 0.17 \pm 0.09$. Granules with $0.5 \geq \alpha \leq 1.4$ were defined as diffusive-like. 2) To establish a transition between modes of motion, the summed Bayesian information criterion for MSD fits to both segments were required to be below –0.4. 3) Owing to constraints of MSD analysis, granule trajectories or trajectory segments shorter than 12 frames (1.2 s) could not be analyzed. Within diffusive-like periods, diffusion coefficients (*D*) were calculated as previously described (Heaslip *et al.*, 2014). The error term for *D* is defined as the square root of the 90% confidence interval (Rausand and Hoyland, 2003).

Trajectory image overlays in Figures 2, 3, and 5 were created by overlaying the trajectories from 10 parasites, which were aligned according to the coordinates of the apical and basal ends of the parasites. Trajectory overlays for Figure 1 were created based on the *x,y* coordinates of each trajectory.

For quantification of the directionality and localization of the directed granule motions, mCherryFP-tubulin was transiently expressed in the SAG1-ΔGPI-GFP parasite line, allowing the unambiguous identification of the parasite's apical end (Supplemental Figure S2A). Directed granule trajectories identified by eye were scored as 1) moving toward the apical end, 2) moving toward the basal end, or 3) moving sideways, that is, off the apical/basal axis of the parasite. Trajectories were also scored as occurring in either the apical end (where MTs were present) or the basal end (where MTs were absent).

TgMyoF protein sequence alignment and analysis

COILS software was used for coiled-coil prediction (www.ch.embnet.org/software/COILS_form.html; Lupas *et al.*, 1991). Sequence alignments were performed using ClustalW multiple-sequence alignment software (www.ebi.ac.uk/Tools/msa/clustalw2).

Creation of *LoxP TgMyoF* parasite line

The *pTKO2_II_3_MyoF_emeraldFP* plasmid was linearized with *Sph*I, and 25 µg was transfected into 1×10^7 *Ku80::diCre* parental parasites (Andenmatten *et al.*, 2013) as described above. Parasites were selected using mycophenolic acid (25 µg/ml) and xanthine (50 µg/ml) until ~70% of the parasites were GFP positive. Clonal parasite lines were obtained by limited dilution into a 96-well plate. After 7 d of growth, wells containing a single plaque were selected for further analysis. All GFP-positive clones were amplified in a six-well plate, and genomic DNA was isolated using the Promega Genomic DNA isolation kit as per the manufacturer's instructions (Promega, Madison, WI). Genomic DNA was analyzed for correct insertion of the pTKO2_II_3_MyoF_emerald plasmid into the TgMyoF genomic locus by PCR (Supplemental Figure S5, A and B, and Supplemental Table S2). All clones containing the correct insertion were further analyzed for their responsivity to rapamycin. Parasites were allowed to invade confluent HFF monolayers for 2 h before treatment with 0.5 µM rapamycin for 30 min. At 72 h after rapamycin treatment, the percentage of emeraldFP-negative vacuoles in each clonal line was determined. A single clone that exhibited ~70% emeraldFP-negative vacuoles was used for all subsequent dense granule imaging experiments. Endogenous TgMyoF-emeraldFP exhibits a diffuse cytosolic localization, as previously shown (Figure 4, B and C; Jacot *et al.*, 2013). The same localization was observed when N-terminally–tagged TgMyoF (eGFP-TgMyoF) was ectopically expressed in parasites (Supplemental Figure S6), indicating that TgMyoF localization is not altered by the fluorescent protein tag. To quantify the level of TgMyoF expression in the parental and *LoxP-TgMyoF* parasites with and without rapamycin treatment, we performed qPCR. RNA was isolated from parental and *LoxP-TgMyoF* parasites 72 h after rapamycin treatment using RNeasy Mini Kit (Qiagen) with on-column DNase digest as per the manufacturer's instructions. cDNA was synthesized using a High-Capacity cDNA reverse transcription kit (Applied Biosystems) as per the manufacturer's instructions. qPCR reaction was performed using SYBR Green Assay. TgMyoF qPCR forward and reverse primers (which bind to sequences encoding the TgMyoF motor domain; Supplemental Table S2) were used to access the level of full-length TgMyoF expression in the parental and untreated *LoxP-TgMyoF* parasites compared with the level of TgMyoF-ΔCT expression in rapamycin-treated *LoxP-TgMyoF* parasites. qRT-PCR results were normalized to beta-tubulin expression accessed with tubulin qPCR forward and reverse primers (Supplemental Table S2). Data are presented as mean value ± SD of six independent biological experiments.

Replication assay

Replication assays were performed as previously described (Heaslip *et al.*, 2010). Parental, *LoxP-TgMyoF* and *TgMyoF-ΔCT* parasites (72 h after rapamycin treatment) were added to coverslips with confluent HFF monolayers and grown for a further 40 h. Samples were fixed and stained for immunofluorescence with the following antibodies: anti-GFP conjugated to Alexa Fluor 488 (diluted 1:500; Life Technologies) to distinguish TgMyoF-emeraldFP–positive/negative vacuoles, anti-HSP60 (diluted 1:1000; Agrawal *et al.*, 2009) as a marker for the apicoplast, and anti-IMC1 (diluted 1:1000) to highlight parasite periphery. The number of parasites/vacuole in

50 vacuoles was determined in parental and *LoxP-TgMyoF* lines. The number of parasites/vacuole in 100 vacuoles was determined in the *TgMyoF-ΔCT* line in each of two independent experiments.

Plaque assay was performed as previously described (Heaslip et al., 2010). Parasites were grown undisturbed for 7 d.

Deconvolution epifluorescence microscopy

To image parasites by immunofluorescence, we collected three-dimensional image stacks at z-increments of 0.3 μm using an Applied Precision DeltaVision imaging station constructed on an Olympus inverted microscope base with a 100×, 1.4 NA oil-immersion lens. Deconvolved images were computed using the point-spread functions and software supplied by the manufacturer. Immunofluorescence samples were prepared as previously described (Heaslip et al., 2011). Antibody concentrations were used as follows: mouse anti-Gra6, 1:2000; mouse anti-IMC1, 1:1000; rabbit anti-GAP45, 1:1000; Mouse anti-AMA1, 1:1000 (Gra6, IMC1 GAP45, and AMA-1 antibodies were a gift from Gary Ward, University of Vermont). Mouse anti-actin (a gift from Markus Meissner, University of Glasgow) was diluted 1:100. Apicoplast and MTs were visualized by transiently expressing pTub8-FNR-RFP (Vollmer et al., 2001) and ptub-GFP-tubulin (Hu et al., 2002) plasmids, respectively. Fixation and permeabilization of parasites' expressed ptub-SAG1ΔGPI-eGFP and ptub-SAG1ΔGPI-mCherryFP resulted in loss of the fluorescent proteins from the PV.

REFERENCES

Agrawal S, van Dooren GG, Beatty WL, Striepen B (2009). Genetic evidence that an endosymbiont-derived endoplasmic reticulum-associated protein degradation (ERAD) system functions in import of apicoplast proteins. J Biol Chem 284, 33683–33691.

Altman D, Sweeney HL, Spudich JA (2004). The mechanism of myosin VI translocation and its load-induced anchoring. Cell 116, 737–749.

Andenmatten N, Egarter S, Jackson AJ, Jullien N, Herman JP, Meissner M (2013). Conditional genome engineering in *Toxoplasma gondii* uncovers alternative invasion mechanisms. Nat Methods 10, 125–127.

Barral DC, Seabra MC (2004). The melanosome as a model to study organelle motility in mammals. Pigment Cell Res 17, 111–118.

Baum J, Gilberger TW, Frischknecht F, Meissner M (2008). Host-cell invasion by malaria parasites: insights from *Plasmodium* and *Toxoplasma*. Trends Parasitol 24, 557–563.

Baum J, Papenfuss AT, Baum B, Speed TP, Cowman AF (2006). Regulation of apicomplexan actin-based motility. Nat Rev Microbiol 4, 621–628.

Besteiro S, Dubremetz JF, Lebrun M (2011). The moving junction of apicomplexan parasites: a key structure for invasion. Cell Microbiol 13, 797–805.

Bougdour A, Durandau E, Brenier-Pinchart MP, Ortet P, Barakat M, Kieffer S, Curt-Varesano A, Curt-Bertini RL, Bastien O, Coute Y, et al. (2013). Host cell subversion by *Toxoplasma* GRA16, an exported dense granule protein that targets the host cell nucleus and alters gene expression. Cell Host Microbe 13, 489–500.

Bougdour A, Tardieux I, Hakimi MA (2014). *Toxoplasma* exports dense granule proteins beyond the vacuole to the host cell nucleus and rewires the host genome expression. Cell Microbiol 16, 334–343.

Braun L, Brenier-Pinchart MP, Yogavel M, Curt-Varesano A, Curt-Bertini RL, Hussain T, Kieffer-Jaquinod S, Coute Y, Pelloux H, Tardieux I, et al. (2013). A *Toxoplasma* dense granule protein, GRA24, modulates the early immune response to infection by promoting a direct and sustained host p38 MAPK activation. J Exp Med 210, 2071–2086.

Bubb MR, Senderowicz AM, Sausville EA, Duncan KL, Korn ED (1994). Jasplakinolide, a cytotoxic natural product, induces actin polymerization and competitively inhibits the binding of phalloidin to F-actin. J Biol Chem 269, 14869–14871.

Bubb MR, Spector I, Beyer BB, Fosen KM (2000). Effects of jasplakinolide on the kinetics of actin polymerization. An explanation for certain in vivo observations. J Biol Chem 275, 5163–5170.

Carruthers V, Boothroyd JC (2007). Pulling together: an integrated model of *Toxoplasma* cell invasion. Curr Opin Microbiol 10, 83–89.

Chuan P, Spudich JA, Dunn AR (2011). Robust mechanosensing and tension generation by myosin VI. J Mol Biol 405, 105–112.

Coppens I, Dunn JD, Romano JD, Pypaert M, Zhang H, Boothroyd JC, Joiner KA (2006). *Toxoplasma gondii* sequesters lysosomes from mammalian hosts in the vacuolar space. Cell 125, 261–274.

Dobrowolski JM, Niesman IR, Sibley LD (1997). Actin in the parasite *Toxoplasma gondii* is encoded by a single copy gene, ACT1 and exists primarily in a globular form. Cell Motil Cytoskeleton 37, 253–262.

Dubremetz JF, Achbarou A, Bermudes D, Joiner KA (1993). Kinetics and pattern of organelle exocytosis during *Toxoplasma gondii*/host-cell interaction. Parasitol Res 79, 402–408.

Foth BJ, Goedecke MC, Soldati D (2006). New insights into myosin evolution and classification. Proc Natl Acad Sci USA 103, 3681–3686.

Frank DJ, Noguchi T, Miller KG (2004). Myosin VI: a structural role in actin organization important for protein and organelle localization and trafficking. Curr Opin Cell Biol 16, 189–194.

Gold DA, Kaplan AD, Lis A, Bett GC, Rosowski EE, Cirelli KM, Bougdour A, Sidik SM, Beck JR, Lourido S, et al. (2015). The *Toxoplasma* dense granule proteins GRA17 and GRA23 mediate the movement of small molecules between the host and the parasitophorous vacuole. Cell Host Microbe 17, 642–652.

Haase S, Zimmermann D, Olshina MA, Wilkinson M, Fisher F, Tan YH, Stewart RJ, Tonkin CJ, Wong W, Kovar DR, et al. (2015). Disassembly activities of actin depolymerization factor (ADF) is associated with distinct cellular processes in apicomplexan parasites. Mol Biol Cell 26, 3001–3012.

Hammer JA III, Sellers JR (2012). Walking to work: roles for class V myosins as cargo transporters. Nat Rev Mol Cell Biol 13, 13–26.

Harding CR, Meissner M (2014). The inner membrane complex through development of *Toxoplasma gondii* and *Plasmodium*. Cell Microbiol 16, 632–641.

He CY, Shaw MK, Pletcher CH, Striepen B, Tilney LG, Roos DS (2001). A plastid segregation defect in the protozoan parasite *Toxoplasma gondii*. EMBO J 20, 330–339.

Heaslip AT, Dzierszinski F, Stein B, Hu K (2010). TgMORN1 is a key organizer for the basal complex of *Toxoplasma gondii*. PLoS Pathog 6, e1000754.

Heaslip AT, Nelson SR, Lombardo AT, Beck Previs S, Armstrong J, Warshaw DM (2014). Cytoskeletal dependence of insulin granule movement dynamics in INS-1 beta-cells in response to glucose. PLoS One 9, e109082.

Heaslip AT, Nishi M, Stein B, Hu K (2011). The motility of a human parasite, *Toxoplasma gondii*, is regulated by a novel lysine methyltransferase. PLoS Pathog 7, e1002201.

Hu K, Johnson J, Florens L, Fraunholz M, Suravajjala S, DiLullo C, Yates J, Roos DS, Murray JM (2006). Cytoskeletal components of an invasion machine—the apical complex of *Toxoplasma gondii*. PLoS Pathog 2, e13.

Hu K, Roos DS, Murray JM (2002). A novel polymer of tubulin forms the conoid of *Toxoplasma gondii*. J Cell Biol 156, 1039–1050.

Jacot D, Daher W, Soldati-Favre D (2013). *Toxoplasma gondii* myosin F, an essential motor for centrosomes positioning and apicoplast inheritance. EMBO J 32, 1702–1716.

Liu J, Wetzel L, Zhang Y, Nagayasu E, Ems-McClung S, Florens L, Hu K (2013). Novel thioredoxin-like proteins are components of a protein complex coating the cortical microtubules of *Toxoplasma gondii*. Eukaryot Cell 12, 1588–1599.

Lupas A, Van Dyke M, Stock J (1991). Predicting coiled coils from protein sequences. Science 252, 1162–1164.

Menetrey J, Bahloul A, Wells AL, Yengo CM, Morris CA, Sweeney HL, Houdusse A (2005). The structure of the myosin VI motor reveals the mechanism of directionality reversal. Nature 435, 779–785.

Morrissette NS, Mitra A, Sept D, Sibley LD (2004). Dinitroanilines bind alpha-tubulin to disrupt microtubules. Mol Biol Cell 15, 1960–1968.

Morrissette NS, Murray JM, Roos DS (1997). Subpellicular microtubules associate with an intramembranous particle lattice in the protozoan parasite *Toxoplasma gondii*. J Cell Sci 110, 35–42.

Morrissette NS, Sibley LD (2002a). Cytoskeleton of apicomplexan parasites. Microbiol Mol Biol Rev 66, 21–38.

Morrissette NS, Sibley LD (2002b). Disruption of microtubules uncouples budding and nuclear division in *Toxoplasma gondii*. J Cell Sci 115, 1017–1025.

Mueller C, Klages N, Jacot D, Santos JM, Cabrera A, Gilberger TW, Dubremez JF, Soldati-Favre D (2013). The *Toxoplasma* protein ARO mediates the apical positioning of rhoptry organelles, a prerequisite for host cell invasion. Cell Host Microbe 13, 289–301.

Nelson SR, Ali MY, Trybus KM, Warshaw DM (2009). Random walk of processive, quantum dot-labeled myosin Va molecules within the actin cortex of COS-7 cells. Biophys J 97, 509–518.

Nissapatorn V (2009). Toxoplasmosis in HIV/AIDS: a living legacy. Southeast Asian J Trop Med Public Health 40, 1158–1178.

Odronitz F, Kollmar M (2007). Drawing the tree of eukaryotic life based on the analysis of 2,269 manually annotated myosins from 328 species. Genome Biol 8, R196.

Olshina MA, Angrisano F, Marapana DS, Riglar DT, Bane K, Wong W, Catimel B, Yin MX, Holmes AB, Frischknecht F, *et al.* (2015). *Plasmodium falciparum* coronin organizes arrays of parallel actin filaments potentially guiding directional motility in invasive malaria parasites. Malar J 14, 280.

Oz HS (2014). Maternal and congenital toxoplasmosis, currently available and novel therapies in horizon. Front Microbiol 5, 385.

Park JJ, Loh YP (2008). How peptide hormone vesicles are transported to the secretion site for exocytosis. Mol Endocrinol 22, 2583–2595.

Pernas L, Adomako-Ankomah Y, Shastri AJ, Ewald SE, Treeck M, Boyle JP, Boothroyd JC (2014). *Toxoplasma* effector MAF1 mediates recruitment of host mitochondria and impacts the host response. PLoS Biol 12, e1001845.

Pruyne D, Legesse-Miller A, Gao L, Dong Y, Bretscher A (2004). Mechanisms of polarized growth and organelle segregation in yeast. Annu Rev Cell Dev Biol 20, 559–591.

Pruyne DW, Schott DH, Bretscher A (1998). Tropomyosin-containing actin cables direct the Myo2p-dependent polarized delivery of secretory vesicles in budding yeast. J Cell Biol 143, 1931–1945.

Rausand M, Hoyland A (2003). System Reliability Theory: Models, Statistical Methods and Applications, Hoboken, NJ: Wiley.

Roos DS, Donald RG, Morrissette NS, Moulton AL (1994). Molecular tools for genetic dissection of the protozoan parasite *Toxoplasma gondii*. Methods Cell Biol 45, 27–63.

Rosowski EE, Nguyen QP, Camejo A, Spooner E, Saeij JP (2014). *Toxoplasma gondii* inhibits gamma interferon (IFN-gamma)- and IFN-beta-induced host cell STAT1 transcriptional activity by increasing the association of STAT1 with DNA. Infect Immun 82, 706–719.

Sahoo N, Beatty W, Heuser J, Sept D, Sibley LD (2006). Unusual kinetic and structural properties control rapid assembly and turnover of actin in the parasite *Toxoplasma gondii*. Mol Biol Cell 17, 895–906.

Salamun J, Kallio JP, Daher W, Soldati-Favre D, Kursula I (2014). Structure of *Toxoplasma gondii* coronin, an actin-binding protein that relocalizes to the posterior pole of invasive parasites and contributes to invasion and egress. FASEB J 28, 4729–4747.

Saxton MJ (1997). Single-particle tracking: the distribution of diffusion coefficients. Biophys J 72, 1744–1753.

Schott DH, Collins RN, Bretscher A (2002). Secretory vesicle transport velocity in living cells depends on the myosin-V lever arm length. J Cell Biol 156, 35–39.

Shastri AJ, Marino ND, Franco M, Lodoen MB, Boothroyd JC (2014). GRA25 is a novel virulence factor of *Toxoplasma gondii* and influences the host immune response. Infect Immun 82, 2595–2605.

Shaw MK, Compton HL, Roos DS, Tilney LG (2000). Microtubules, but not actin filaments, drive daughter cell budding and cell division in *Toxoplasma gondii*. J Cell Sci 113, 1241–1254.

Skillman KM, Daher W, Ma CI, Soldati-Favre D, Sibley LD (2012). *Toxoplasma gondii* profilin acts primarily to sequester G-actin while formins efficiently nucleate actin filament formation in vitro. Biochemistry 51, 2486–2495.

Skillman KM, Diraviyam K, Khan A, Tang K, Sept D, Sibley LD (2011). Evolutionarily divergent, unstable filamentous actin is essential for gliding motility in apicomplexan parasites. PLoS Pathog 7, e1002280.

Striepen B, He CY, Matrajt M, Soldati D, Roos DS (1998). Expression, selection, and organellar targeting of the green fluorescent protein in *Toxoplasma gondii*. Mol Biochem Parasitol 92, 325–338.

Sweeney HL, Houdusse A (2007). What can myosin VI do in cells? Curr Opin Cell Biol 19, 57–66.

Travier L, Mondragon R, Dubremez JF, Musset K, Mondragon M, Gonzalez S, Cesbron-Delauw MF, Mercier C (2008). Functional domains of the *Toxoplasma* GRA2 protein in the formation of the membranous nanotubular network of the parasitophorous vacuole. Int J Parasitol 38, 757–773.

Trybus KM (2008). Myosin V from head to tail. Cell Mol Life Sci 65, 1378–1389.

Tumbarello DA, Kendrick-Jones J, Buss F (2013). Myosin VI and its cargo adaptors—linking endocytosis and autophagy. J Cell Sci 126, 2561–2570.

van den Hoff MJ, Moorman AF, Lamers WH (1992). Electroporation in "intracellular" buffer increases cell survival. Nucleic Acids Res 20, 2902.

Vollmer M, Thomsen N, Wiek S, Seeber F (2001). Apicomplexan parasites possess distinct nuclear-encoded, but apicoplast-localized, plant-type ferredoxin-NADP$^+$ reductase and ferredoxin. J Biol Chem 276, 5483–5490.

Xu C, Min J (2011). Structure and function of WD40 domain proteins. Protein Cell 2, 202–214.

Zajac AL, Goldman YE, Holzbaur EL, Ostap EM (2013). Local cytoskeletal and organelle interactions impact molecular-motor-driven early endosomal trafficking. Curr Biol 23, 1173–1180.